J Therm Spray Tech
DOI 10.1007/s11666-017-0662-2

PEER REVIEWED

Microstructural Evolution in Solution Heat Treatment of Gas-Atomized Al Alloy (7075) Powder for Cold Spray

A. Sabard[1] · H. L. de Villiers Lovelock[2] · T. Hussain[1]

Submitted: 17 July 2017 / in revised form: 17 October 2017

Abstract Cold gas dynamic spray is being explored as a repair technique for high-value metallic components, given its potential to produce pore and oxide-free deposits of between several micrometers and several millimeters thick with good levels of adhesion and mechanical strength. However, feedstock powders for cold spray experience rapid solidification if manufactured by gas atomization and hence can exhibit non-equilibrium microstructures and localized segregation of alloying elements. Here, we used sealed quartz tube solution heat treatment of a precipitation hardenable 7075 aluminum alloy feedstock to yield a consistent and homogeneous powder phase composition and microstructure prior to cold spraying, aiming for a more controllable heat treatment response of the cold spray deposits. It was shown that the dendritic microstructure and solute segregation in the gas-atomized powders were altered, such that the heat-treated powder exhibits a homogeneous distribution of solute atoms. Micro-indentation testing revealed that the heat-treated powder exhibited a mean hardness decrease of nearly 25% compared to the as-received powder. Deformation of the powder particles was enhanced by heat treatment, resulting in an improved coating with higher thickness ($\sim$ 300 µm compared to $\sim$ 40 µm for untreated feedstock). Improved particle–substrate bonding was evidenced by formation of jets at the particle boundaries.

Keywords Cold spray · Aluminum alloy · 7075 · Solution heat treatment · Powder heat treatment

Introduction

Cold spray is a relatively new material deposition process exploiting mainly the kinetic energy of fine powder particles to achieve a dense coating or deposit on a target substrate surface. Powder particles are introduced in a high-velocity gas stream which accelerates them toward a substrate without melting them (Ref 1-3). The powder undergoes high strain rate plastic deformation upon impact and bonds with the target surface and/or with the previously deposited layers of material. The potential of cold spray processing for dimensional restoration as well as structural repair of light metallic alloys (Al, Mg and Ti mainly) has been extensively studied (Ref 4). The specific build-up mechanisms of cold spraying, which usually imparts a high degree of work hardening to the powder particles (Ref 5) and post-deposition residual stresses (Ref 6, 7), can lead to low-ductility coatings. Post-deposition heat treatments have been shown to improve the properties (Ref 8, 9, 10, 11).

Cold spraying of aluminum alloys is particularly interesting for various repair applications in the aerospace, automotive and defense sectors. In the case of aluminum alloys, it has been shown that the rapid solidification experienced by gas-atomized powders during manufacture

This article is an invited paper selected from presentations at the 2017 International Thermal Spray Conference, held June 7–9, 2017, in Düsseldorf, Germany, that has been expanded from the original presentation.

✉ T. Hussain
tanvir.hussain@nottingham.ac.uk

A. Sabard
emxas4@nottingham.ac.uk

[1] Faculty of Engineering, University of Nottingham, Nottingham NG7 2RD, UK

[2] TWI Ltd, Granta Park, Great Abington, Cambridge CB21 6AL, UK

Published online: 16 November 2017

can lead to a variety of non-equilibrium microstructures (Ref 12, 13). The exposure of homogenized liquid melt to a cold gas stream results in the droplets being subjected to extremely high cooling rates (up to 10^8 K s^{-1}). Combined with the temperature gradient within each particle during solidification, this leads to a cellular dendritic microstructure. The solidifying dendrites propagate through the material, releasing heat in a phenomenon called recoalescence (Ref 14). The solidification of the droplet in contact with the cold gas, combined with this temperature increase in the droplet, results in a non-equilibrium microstructure. There is usually also a significant localized segregation of alloying elements associated with the dendrites (Ref 15, 16). Powders are subjected to a range of cooling rates (10^{-4} to 10^{-8} K s^{-1} Ref 17) during solidification, and this is partially related to the powder size, with smaller particles experiencing faster cooling rates due to their larger surface area-to-volume ratio and smaller overall mass. This variation in cooling rate leads to a wide range of microstructures in atomized powders (Ref 18). It affects the secondary dendritic arm spacing (Ref 19, 20) and thus the intensity of the solute segregation.

This inconsistency of microstructure and elemental distribution in the powder particles could be detrimental in terms of reproducibility of the coatings as well as potential response to heat treatment. For example, grain growth during post-spray annealing of cold-sprayed coatings was found to be limited by the presence of grain boundary solute segregation of cold-sprayed 7075 aluminum alloy (Ref 21). High-temperature heat treatments could reduce alloying element segregation and/or work hardening in cold spray deposits, but applying high-temperature heat treatments to repaired components is undesirable in many situations. Hence, to reduce or even eliminate the alloying element segregation, solution heat treatment of the powder has been considered here in the case of AA7075, a lightweight Al–Zn–Mg–Cu alloy widely used in the aerospace industry. Solution heat treatment corresponds to the process of heating a material below its melting range for a specific time and within the single-phase region in order to allow crystals and atoms to diffuse evenly throughout the aluminum (Ref 22). The non-uniformly distributed alloying elements throughout the grain structure are expected to be redissolved into solid solution (Ref 23), homogenizing the microstructure and decreasing the hardness (Ref 24). However, the main aim of this heat treatment is not only to reduce solute segregation and decrease hardness (or increase ductility) but also to offer the potential of post-deposition heat treatment (age hardening) of the deposits, via a controlled precipitation of the constituents.

In this study, the solution heat treatment of a gas-atomized 7075 series aluminum alloy powder was performed using a novel technique, as described below, and the particles were then quenched in order to obtain the desired microstructure. The microstructure following heat treatment was analyzed using electron microprobe and backscattered SEM imaging, and the effect of the element distribution modification and the altered powder particle properties on the cold spray deposition was then observed using swipe and coating build-up tests, which were conducted onto an AA6061 substrate.

Experimental Methods

Materials

A spherical gas-atomized AA7075 powder (Valimet Inc, USA), having a Dv10, Dv50 and Dv90 of 17, 34, and 60 μm, respectively, was the feedstock material of this study. The chemical composition of the powder was 5.72 wt.% Zn, 1.69 wt.% Cu, 2.30 wt.% Mg, 0.20 wt.% Cr, 0.17 wt.% Fe, 0.03 wt.% Mn and 0.13 wt.% Si. The substrates used for the cold spray experiments were 3-mm-thick 6061-T6 (Al–Si–Mg) aluminum alloy plates (30 × 100 mm).

Solution Heat Treatment and Quenching of the Powder Feedstock

The as-received feedstock powders were sealed in a quartz tube prior to their introduction into the furnace. Once the particles were inserted in the vial, a 10-mPa vacuum was created using a diffusion pump; then, the tube was carefully closed and sealed using an oxy- propane flame. The dimensions of the tube were as follows: outer diameter 14 mm, length ~ 100 mm and 2 mm wall thickness. Al alloy powders can potentially explode in the presence of oxygen and ignition sources, and hence, the heat treatment was performed under vacuum in the tube to mitigate the fire risk. Solution heat treatment of the powder was carried out using a commercial box furnace at 450 °C for 4 h. The temperature of the powder was assumed to reach the furnace temperature, and therefore, the temperature of the powder itself was not measured. However, the temperature of the vial post-quench was measured using a thermocouple and had cooled down at room temperature after 180 s. The temperature was chosen following the standard T6 (solution heat treatment + artificial aging) treatment performed on AA7075. The quartz tube was then quenched into cold water (5 °C) and kept submerged for 5 min until the powder particles had reached room temperature. The container was opened using a cutting wheel to remove the top of the tube and the powder collected into a container. The solution heat treatment experiment was performed in two batches of 140 g of AA7075 powder each.

Cold Spray Deposition: Swipe Tests and Coating Deposition

The cold spray experiments were performed using a custom-made high-pressure cold spray system at the University of Nottingham using helium as the primary accelerating gas in order to achieve high impact velocities of the incident particles. The rig setup has been described in detail elsewhere (Ref 25). Cold spray deposition was carried out onto AA6061 substrates while maintaining a He gas pressure of 2.9 MPa at room temperature with a high-pressure commercial powder feeder (Praxair 1264 HP, Indianapolis, IN, USA). A hardened stainless steel nozzle was used for the experiments, having an expansion ratio of 8 with a divergent length of 150 mm. Particles were sprayed using a nozzle stand-off distance of 20 mm. Swipe tests were conducted in order to observe the impact of single particles onto the substrate by using a traverse speed of 600 mm/s and a single pass. Further cold spraying coating deposition experiments were performed at a traverse speed of 100 mm/s to deposit coatings. The substrates were ground with a P240 SiC paper for the coating deposition, whereas the swipe tests were performed on substrates that were ground with different grade SiC papers to a 1200-grit finish and polished with 6 and 1 μm diamond paste in order to give them a mirror finish. The coating deposition was performed with 8 passes of the gun over the substrates to build a deposition area of 12 by 30 mm on the substrates.

Microstructural Analysis

The microstructure of both the as-received and solution heat-treated powders and cold-sprayed coatings was evaluated using optical microscopy (OM—Eclipse LV100ND, Nikon Corporation, Japan) and scanning electron microscopy (SEM—JEOL JSM 6490LV, JEOL Ltd., Japan). The surface images of the powder and coatings were taken at 10 kV in secondary electron (SE) mode, whereas the images in cross section were obtained using an accelerating voltage of 20 kV in SE and BSE (backscattered electron) modes. The images taken at 10 kV were meant to give more surface information for the top-view of the particles, due to a smaller interaction volume, whereas the 20-kV accelerating voltage was more suitable for the microstructural analysis due to its larger interaction volume. The SEM images of the particle impacts after the swipe tests were taken with the samples tilted at 45° in order to have a side view of the particle bonded to the substrate. Electron probe micro-analysis (EPMA—Superprobe JEOL JXA 8200, JEOL Ltd., Japan), operated at 30 kV, was performed on individual powder particles to obtain a high-resolution elemental mapping using wavelength dispersive spectroscopy (WDS). The particle size analysis was measured by laser diffractometry (Laser Mastersizer 3000, Malvern Instruments, Malvern, UK) in dry environment. OM, SEM and EPMA samples were prepared using standard metallographic techniques. All of the samples were sectioned using a precision saw at a cutting speed of 0.005 mm/s. The powders and cold spray deposits were cold mounted in EpoFix® resin (Struers, UK). Powders were ground with P1200 silicon carbide paper to avoid losing too much material, whereas cold spray deposits were sequentially ground using P240, P400, P800 and P1200. Both powders and deposits were then polished with 6 and 1 μm diamond paste, and the final polish performed using a colloidal silica (0.06 μm) suspension. For optical microscopy, samples were chemically etched using Keller's reagent (95 mL of H_2O, 2.5 mL HNO_3, 1.5 mL HCl, 1.0 mL HF) for 5 s.

Image Analysis

The fraction of deposition and the average size of deposited particles were measured using thresholds on 3 different SEM top-view SE images of each sample. A total surface of 3.0 × 4.8 mm was used for the measurements, using ImageJ (US National Institute of Mental Health, MD) software.

Microhardness Measurement

The microhardness analysis was performed using a MMT-7 Vickers Microhardness instrument (Buehler, IL, USA). Each sample underwent 8 measurements. A 10-gf load was applied for 10 s for mounted particles in cross-section.

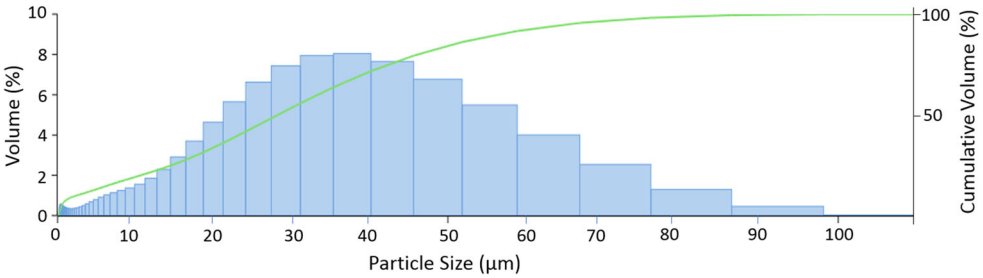

Fig. 1 Bimodal particle size distribution measured by laser diffractometry showing a large number of particle above 30 μm of diameter

Results

Microstructure of As-Received AA7075 Powder

The particle size of the gas-atomized powder (Fig. 1) exhibits a Gaussian-type distribution. The measured Dv10, Dv50 and Dv90 were, respectively, 2.5, 28, and 57 µm. The topography of the as-received powders in the SEM SE image (Fig. 2) shows fine satellites on top of large particles. The powder has a mostly spherical microstructure with some irregular particles, possibly due to solidification before they could coalesce into a spherical shape. This satelliting effect, commonly observed among gas-atomized powder, can be explained by the in-flight contact of small size partially solidified droplets with larger solidified particles (Ref 26).

When examined by optical microscopy, the gas-atomized powder (Fig. 3a) shows a spherical morphology containing a mixture of both large and small particles. The microstructure of the material is revealed by Keller's etchant (Fig. 3b) and has small dendritic cells whose size varies between 1 and 4 µm. This commonly observed microstructure of gas-atomized aluminum alloy powder has been attributed to several phenomena occurring during the powder manufacturing process such as solidification and cooling rate, thermal equilibration and partial re-melting of solid particles, as well as the presence of pre-solidified micro-droplets and dendrite fragments (Ref 27). During solidification of the powder, the growth of the α-Al dendrites is accompanied with a solute rejection (Ref 28). The solute elements are segregated on the sides of the dendrites and encounter each other, forming the dendritic cells that we can observe (Ref 29). The average cooling rate of aluminum powder prepared by atomizing varies between 10^4 and 10^7 K/s, with the temperature of the small particles decreasing faster. This wide range of cooling rates leads to different distributions and shapes of cells in the powder particles. The smallest ones, observed in the optical micrographs (Fig. 3), showed relatively small dendritic cells, attaining around 1 µm, whereas larger particles, having a diameter of 40 µm, exhibit larger dendritic cells, 2-3 µm wide. A different behavior was also noticed in the case of a particle of a diameter of 20 µm where the dendritic structure was only noticed on one side of the droplet, explained by a cooling rate high enough to solidify the particle in some areas before the growth of the dendrites.

When examined by SEM in SE and BSE modes, the as-received AA7075 powder shows a non-uniform distribution of solute elements. A typical example showing a 40-µm-sized particle can be seen in Fig. 4. The SE image shows the dendritic cells within the powder particles, and the BSE image reveals a compositional variation within the particle (due to variation in contrast in the BSE image where contrast depends on the mean atomic number of the elements). In fact, the brightness difference between the matrix and the interdendritic regions indicates the possible

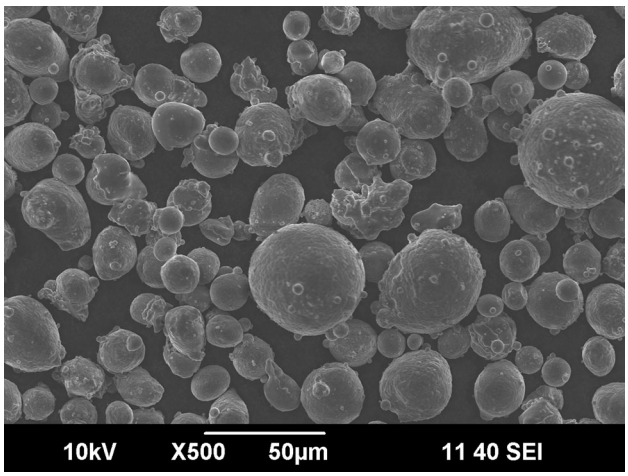

Fig. 2 Topography of the as-received AA7075 showing a mostly spherical morphology with some satellite particles

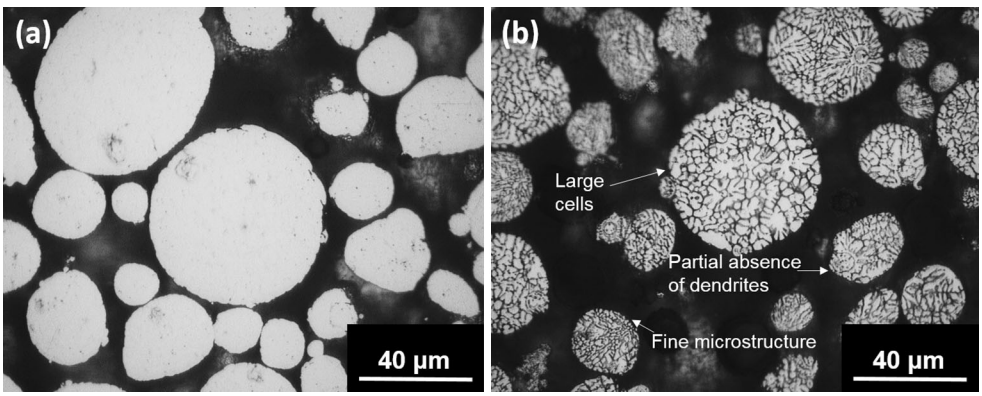

Fig. 3 Optical micrographs of the cross section of gas-atomized AA7075 powder unetched (a) and after etching for 5 s with Keller's etchant (b) revealing a dendritic microstructure

presence of the solute atoms, especially Zn and Cu at the dendritic cell boundaries.

The EPMA presented in Fig. 5 reveals the distribution of the main solute atoms—i.e., Zn, Cu, Mg, Fe—in the as-received AA7075 powder. The red color on the microprobe scans indicates a relatively high concentration of the material, whereas the blue color shows a low concentration of the scanned element. The results confirm the presence of those alloying elements at the dendritic cell boundaries. Although the dendritic cell boundaries are enriched in alloying elements, intermetallic phases such as $Mg(Zn,Cu,Al)_2$ (Ref 30), Al_2CuMg (Ref 31) or Mg_2Si (Ref 30), commonly observed and previously reported in this alloy, could not be conclusively confirmed due to the

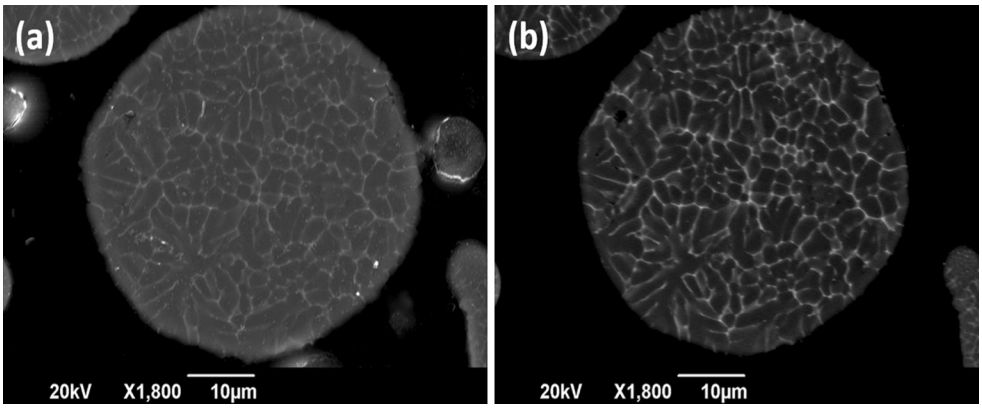

Fig. 4 SEM micrographs of an as-received AA7075 particle in cross section, in secondary electrons (a) and backscattered electrons (b), revealing a composition variation between interdendritic regions and matrix

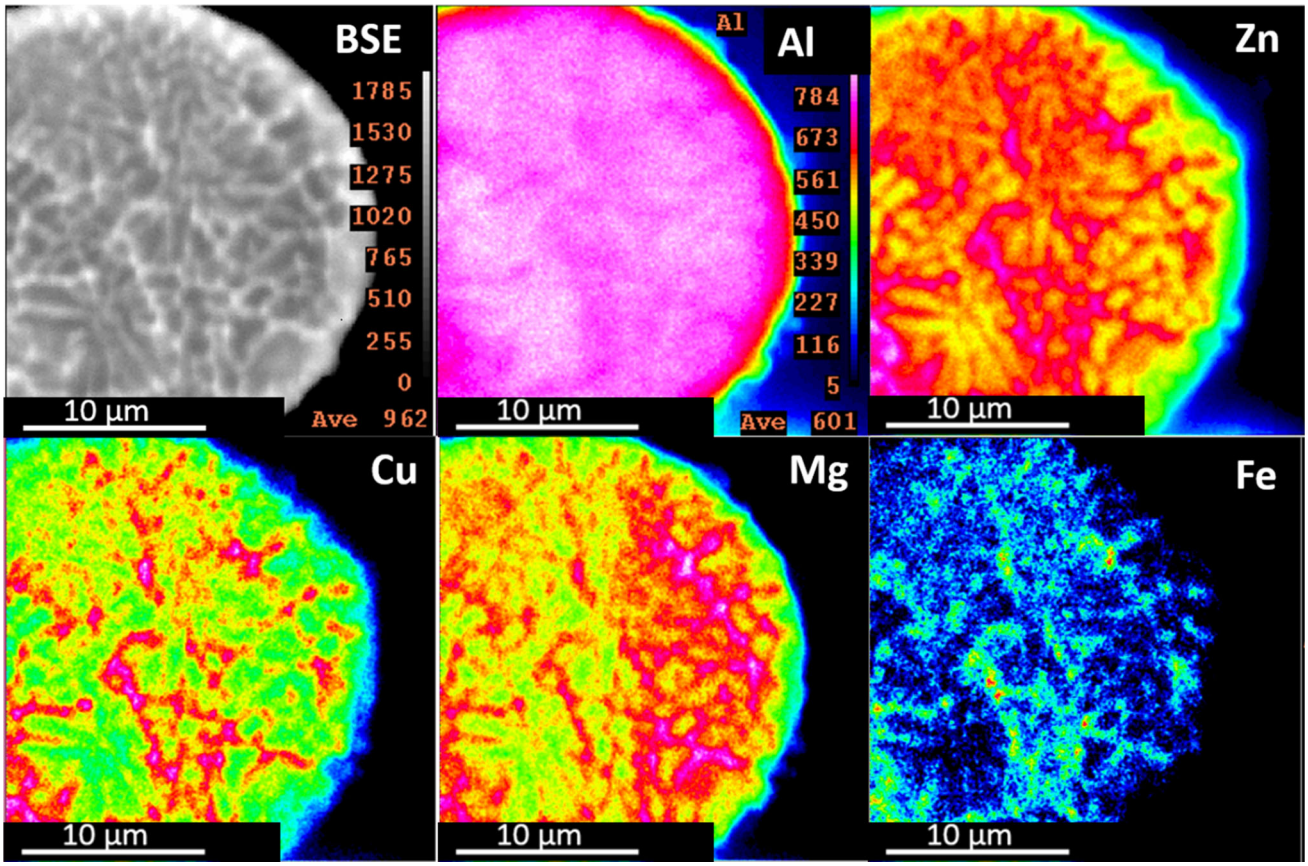

Fig. 5 EPMA-WDS map of as-received gas-atomized AA7075 powder showing the solute segregation occurring in the interdendritic regions

resolution limitation of the microprobe and the high solute segregation hiding other phases. Cu and Fe appear to follow the same distribution in the particle, whereas the Zn and Mg concentration is more dispersed into the inter-dendritic regions. Al seems to be homogeneously distributed throughout, despite slight variations of content between the dendritic cell boundaries and the cores of the dendritic cells.

Microstructure of Solution Heat-Treated AA7075 Powder

Unetched particles of AA7075 powder after solution heat treatment show no clear differences with the as-received powder in cross section (Fig. 3a and 6a), except a slight increase in terms of porosity within the particles (white arrows), possibly explained by the preferential melting (insipient melting) of certain phases during the solution heat treatment, or due to dissolved or trapped gas in the droplet released during solution heat treatment. On the other hand, etching reveals that the dendritic structure of the as-received powder has disappeared following heat treatment (Fig. 3b and 6b). Now, clear differences can be observed in the powder between the smallest and the largest particles, such as the uniform bright contrast showed by the smaller particles. The original inconsistency of dendritic distribution observed in the as-received powder presumably led to these differences, enhanced by possible etching artifacts. The SE and BSE images (Fig. 7) reveal different features and differentiate from the etched optical micrographs observed previously. The lack of contrast in the BSE image highlights that the solute atoms have been dissolved into solid solution and that the matrix has been largely homogenized. A few precipitates can also be observed on the cross-section of the particle. Needle-shaped bright precipitates are numerous in the microstructure, as well as smaller spherical dark areas, both being too small to be identified using EDS.

The elemental composition in the microprobe analysis (Fig. 8) helps identify the different phases observed in the microstructure. High concentrations of Cu and Fe are still observed in the microstructure of the solution heat-treated particle. The needle-shaped precipitates distinguished in the BSE image (Fig. 7) are now identified as mostly composed of those two solute elements. Some larger phases of the same composition, exhibiting much more random shapes, not detected in the BSE image, can be also seen in the particle. The matrix itself shows a mostly homogeneous mixture of Al and Zn, potentially in a supersaturated solid solution induced by the heat treatment conducted on the batch of powder. A slight agglomeration of Mg is distinguished, possibly related to the black spherical phase observed previously in the BSE scan of the solution heat-treated particle.

Microhardness Measurement of the Particles

The solution heat treatment of the AA7075 particles prior to spraying was performed partly to increase the ability of the powder to plastically deform upon impact in cold spraying. Microhardness measurements were thus taken on the AA7075 particles, as-received and after solution heat treatment. The as-received powder (Table 1) shows a microhardness of 101 HV $\pm$ 5.74, and the solution heat-treated powder exhibits a 25% decrease in microhardness, at 75.2 HV $\pm$ 4.98. This significant decrease in microhardness of the supersaturated solid solution shows good potential for cold spray, and the powder after heat treatment is believed to be more amenable for this solid-state deformation process. As a reference, a typical AA7075-T6 bulk microhardness is between 165 and 175 HV.

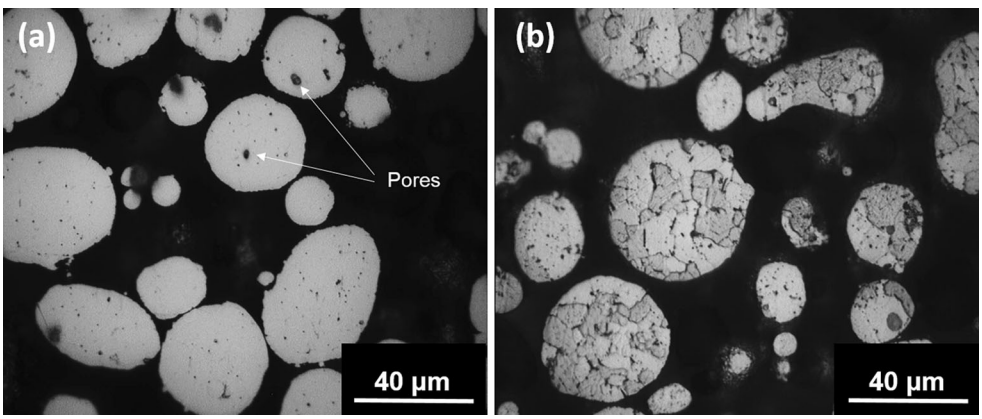

Fig. 6 SEM micrographs of an as-received AA7075 particle in cross section. Secondary electrons (a) and backscattered electrons (b) revealing a dissolution of the dendrites after heat treatment

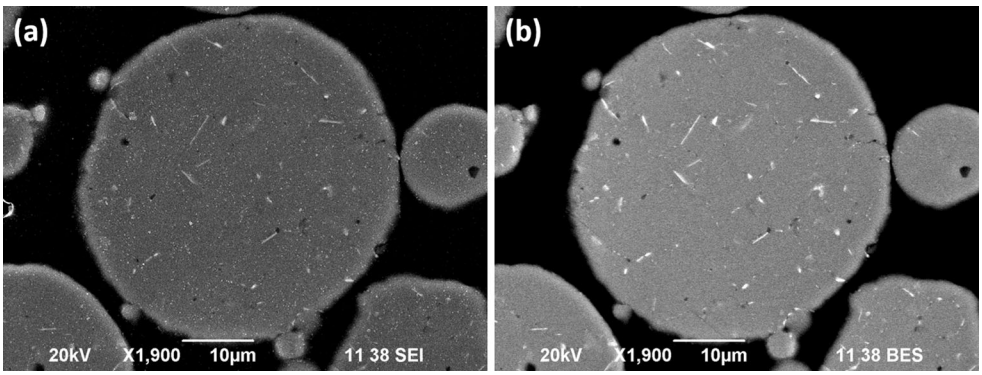

Fig. 7 SEM micrographs of a solution heat-treated AA7075 particle. SE (a) and BSE (b) revealing a homogeneous microstructure and coarse needle-shaped precipitates

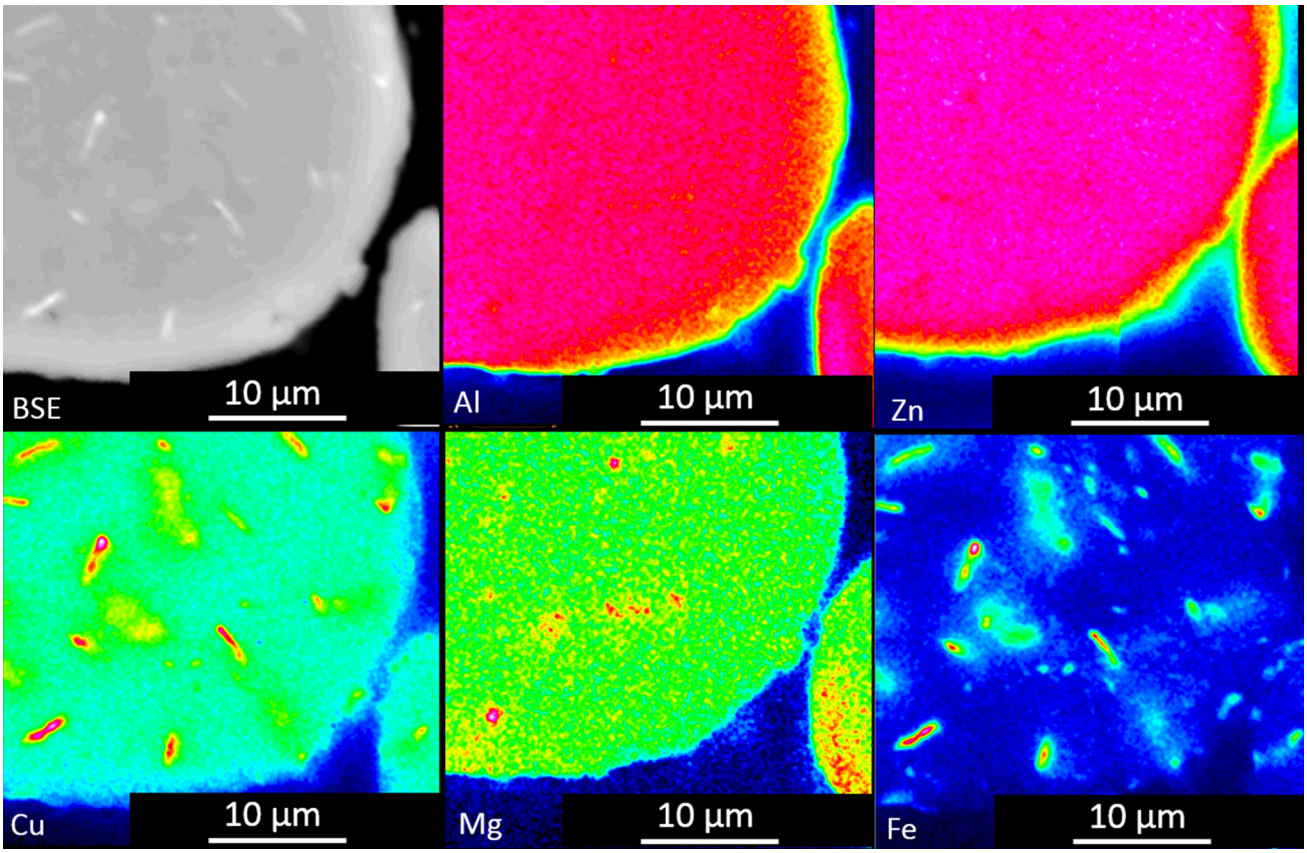

Fig. 8 EPMA-WDS map of a solution heat-treated AA7075 particle revealing a Al-Zn matrix and the presence of Cu- and Fe-rich phases

Table 1 Microhardness measurements of AA7075 powder

Material	As-received powder	Solution heat-treated powder
Microhardness (HV)	101 ± 5.74	75.2 ± 4.98

Individual Particle Deformation During Swipe Tests

The top-view of the swipe tests realized with both as-received and heat-treated powder (Fig. 9) is a good illustration of the behavior of the particles upon impact on the substrate. A clear difference is observed between the two different batches, such as the fraction of deposition. Numerous craters are observed in the case of the as-received powder, illustrating the rebounding effect of the particles. On the other hand, the solution heat-treated particles show a much better adhesion to the substrate, even though craters can still be observed on the surface of the AA6061 substrate, albeit at a lower percentage. Table 2 illustrates these observations by quantifying the fraction of

deposition (which is a ratio of particle deposited versus craters on the polished surface). These measurements support the SEM images seeing previously, the solution heat-treated powder showing a fraction of deposition of almost 50% as opposed to 8.6% for the as-received one. The average size of the deposited particles has also been measured and reveals that the diameter measured on the top-view is slightly bigger in the case of the solution heat-treated powder (32.1 ± 8.3 versus 27 ± 11.1 μm). Both of those diameters are smaller than the Dv50 of the particles. Although there are limitations in measuring mean deposited particle diameters from the topography of the swipe tested samples due to various levels of particle deformation, the results, however, show that there are only minor differences between the mean diameters of the as-received and solution heat-treated feedstock. Hence, the fivefold increase in fraction of deposition cannot be attributed to the particle size effect, which dictates the so-called critical velocity. This increase in fraction of deposition is likely to be due to the changes in intrinsic particle microstructure and mechanical properties as a consequence of the solution heat treatment.

The bonding of the particles on the substrate, and the way they behave upon impact, are illustrated by the 45° tilted SEM images (Fig. 10) which reveal different deformation of the two batches. Figure 10(a) and (b) illustrates that the particles kept a rather spherical shape showing poor particle deformation upon impact. A poor bonding seems to be observed, illustrated by the gap below the particle in the top-left image. In fact, the particle seems to be on the verge of bouncing back due to weak bonding with the substrate. The powder particle is partially embedded in the substrate, and most the deformation seems to have been undergone by the substrate. On the other hand, the solution heat-treated particles illustrated in Fig. 10(c) and (d) have undergone a much more intense deformation, illustrated by the flattened "splat" shape of the powder after impact. Apart from the shape, a ring of jet type morphology can be observed around the impact zone, as well as few fragments of the deposited material, ejected upon impact of the particle with the substrate.

Cold Spray Coating Deposition

After observing the bonding of the individual particle with the substrate, the way the particles adhere to each other was investigated by performing cold spray deposition with the as-received (Fig. 11a) and solution heat-treated (Fig. 11b) powder. For the exact same spraying parameters, the difference between the two coatings is clear. Indeed, the 8 passes sprayed onto the AA6061 substrate resulted in less than 40 μm of deposition in the case of the as-received powder. It is, however, important to notice the deformation of the substrate despite the poor deposition efficiency, as well as a few particles well embedded in the substrate. No gap is observed between the deposited layer and substrate, but a crack seems to be present in between the particles, indicating poor particle–particle bonding. On the other hand, the coating deposited using the heat-treated powder (Fig. 11b) was almost 300 μm thick. Again, no gap is observed at the coating–substrate interface, but a small crack is observed at the bottom-left corner of the figure and is present mostly within the coating. A small amount of porosity can also be seen within the coating at the particle–

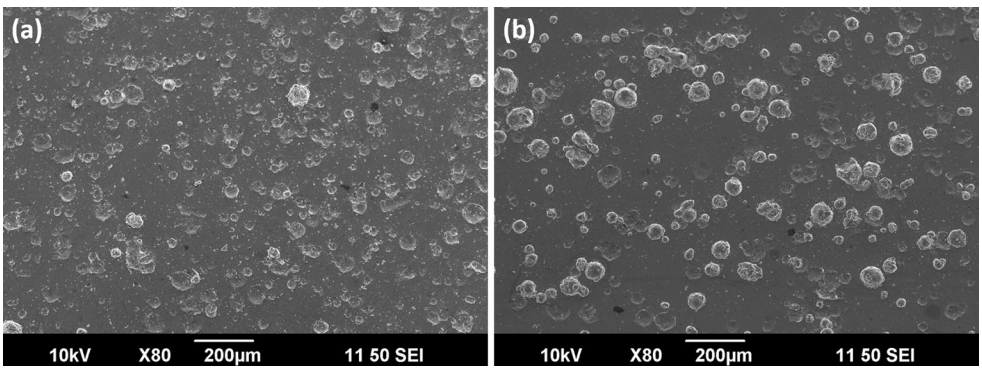

Fig. 9 Cross section of deformed as-received (a) and solution heat-treated (b) particles onto AA6061 after swipe tests showing a high number of craters and a low fraction of deposition in the case of the as-received powder

Table 2 Fraction of deposition and size of deposited particles using top-view SEM images

Material	As-received powder	Solution heat-treated powder
Deposition versus crater fraction	8.6%	49.6%
Average size of deposited particles (μm)	26.74 ± 8.3	32.1 ± 11.1

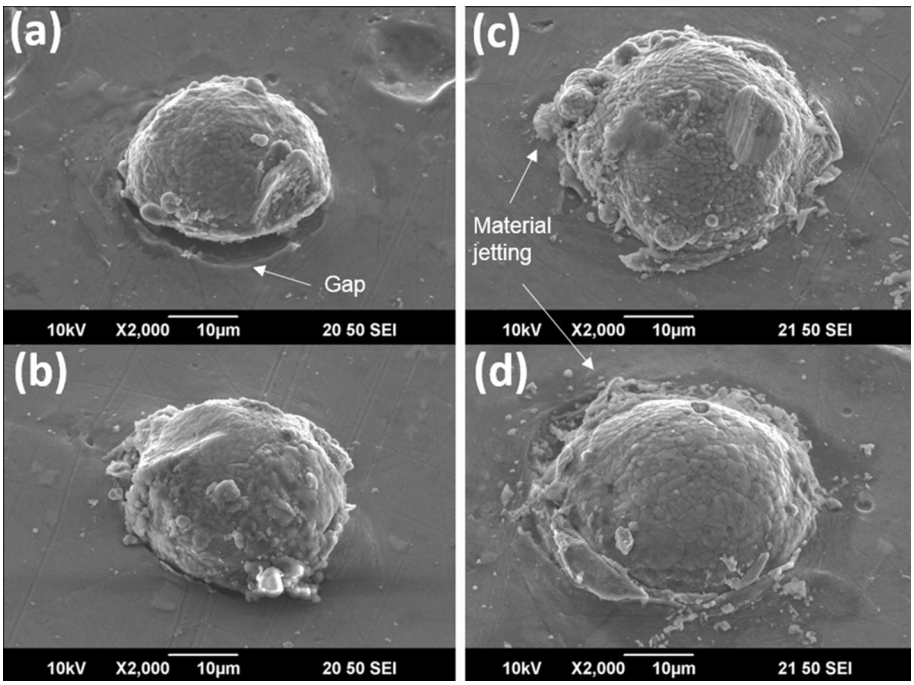

Fig. 10 SE picture of the top surface of individual as-received (a-b)) and solution heat-treated (c-d) AA7075 particle after spraying revealing a better particle–substrate bonding in the case of the solution heat-treated powder

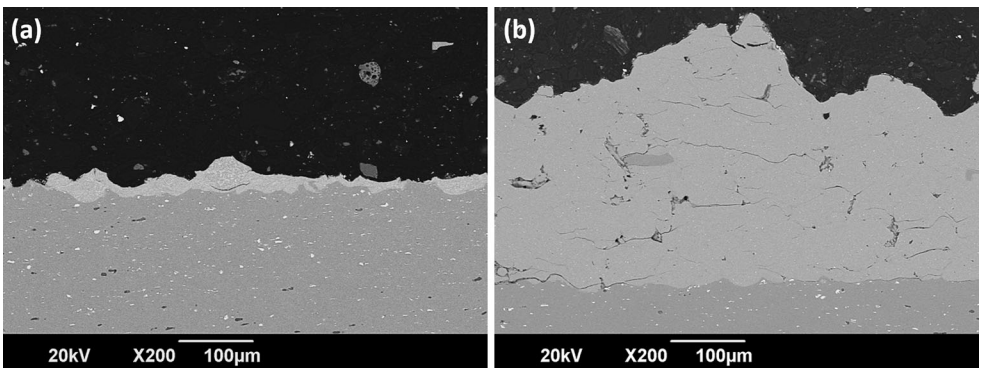

Fig. 11 Cross section BSE images of the coating deposition of as-received particles (a) and solution heat-treated (b) and of AA7075 powder showing a high thickness (300 µm) in the second case

particle interfaces. Images of those coatings at higher magnification (Fig. 12) allow a better view of the deformation undergone by the material. The image of the coating of as-received particles shows a large particle of almost 50-µm diameter, where few smaller particles have impacted (Fig. 12a). A gap is noticed in between the powder particles, illustrating the weak bonding in some areas of the top layer. However, the high magnification image of the coatings deposited using the heat-treated powder reveals a closer bond between the particles, which makes it harder to distinguish the boundaries between them (Fig. 12b). The precipitates observed in the heat-treated powder (Fig. 7) are also present in the as-deposited coating, with the higher coating density possibly related to a greater degree of deformation of the impacted particles.

The coating–substrate interfaces reveal similar behavior in both cases (Fig. 13) when viewed at higher magnification using BSE imaging. In both cases, good bonding seems to be present between the particles and the substrate. Even a partial mixing of the powder with the AA6061 substrate (white arrow) occurred indicating a good bonding due to interfacial mixing and the well-established mechanical interlocking mechanisms (Ref 32). In terms of microstructure, the dendritic structure of the as-received particles in the coating illustrates the deformation of the particle. The first layer, in contact with the substrate, exhibits a fine microstructure, which becomes hard to distinguish, whereas the particle located at the top shows larger dendritic cells with a tendency to deform in a longitudinal direction due to successive impacts by incoming particles.

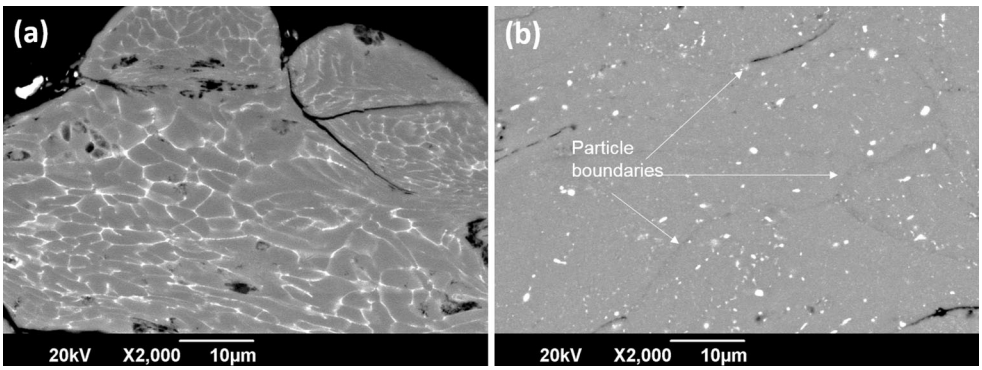

Fig. 12 Higher magnification of deformed particles into the coating of as-received (a) and solution heat-treated particles (b) illustrating the high deformation undergone by the particles during deposition

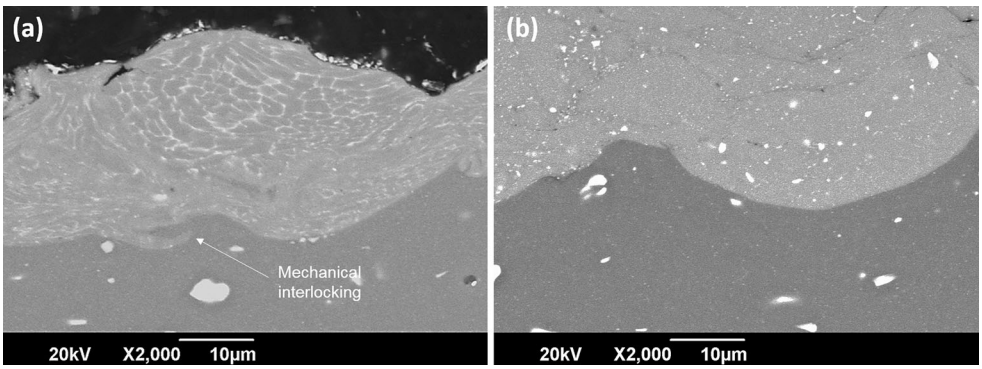

Fig. 13 BSE images of the bonding between the deposit and the substrate in both cases: As-received (a) and solution heat-treated (b) AA7075 powder. A mechanical interlocking is observed between the substrate and the coating

Discussion

The powder modification will be discussed first in this section, and the effect of the heat treatment on the non-equilibrium microstructure of the gas-atomized aluminum alloy powder will be described and analyzed thereafter. Finally, the effect of this microstructure modification on the coating deposition will be discussed.

Microstructural Modification of Powder Feedstock During Heat Treatment

The cooling rates reached during the gas atomization process due to the high relative velocity between the droplets and the fast-moving cold gas stream lead to specific microstructures within the atomized particles, due to various cooling rates depending on the particle diameters. Undercooling is achieved after the contact between the molten droplets and the cooling gas during solidification, and the droplets are cooled well below the solidus temperature before nucleation and crystallization is initiated (Ref 33). In these conditions, the material is far from being thermodynamically stable and non-equilibrium microstructures are formed, as evidenced by the dendritic structure in the majority of rapidly solidified aluminum alloys (Ref 12). The following equation (Ref 34) has been proposed to associate the dendritic cell area with the solidification rate:

$$v = \left(\frac{A}{d}\right)^{\frac{1}{n}} \quad \text{(Eq 1)}$$

where d is the measured dendrite parameter in µm, calculated as the square root of the average dendrite cell area, v is the cooling rate in K s^{-1}, and A and n are constants (Ref 34). A relates to alloy properties, and $A = 100$ in case of high-strength aluminum alloys, whereas $n = 1/3$ for equiaxed grains (Ref 34). Calculations can be done to get an approximation of the cooling rates reached for the material of this study. In the case of a 40-µm particle (Fig. 4), a cooling rate of around 9.2×10^4 K s^{-1} is obtained, whereas a cooling rate of around 3.3×10^5 K s^{-1} is calculated in the case of a 15-µm particle similar to the one observed in Fig. 3. These measurements are based on the dendritic cell area, and a variation of few micrometers between the size of the small and large particles' cells is explained by a fairly high difference of cooling rates, according to Eq 1. Studies even revealed the presence of a non-dendritic structure for sufficiently small particles in

gas-atomized aluminum alloy powders (Ref 18), due to the high number of nucleation sites induced by a deep pre-solidification undercooling (Ref 35). This phenomenon was only sporadically observed in our case, potentially because the cooling rates required for this process to happen were not easily attained during the powder manufacturing process. It was partially observed in one of the small particles shown in Fig. 3, exhibiting only small dots rather than dendrites on its left-hand side. It could be explained by some in-flight contact between particles during solidification, altering the cooling rate by rapid heat transfer between them and leading to those ultra-fine microstructures (Ref 18). This inconsistency of microstructure in gas-atomized aluminum alloy powder is accompanied by solute segregation (Fig. 4). When the alloy is not cooled down below the solidus quickly enough, diffusion occurs during solidification, leading to a migration of the solute atoms toward the grain boundaries (Ref 15). This segregation occurring during gas atomization and the movement of elements is confirmed by a fine dispersion of solute atoms in the interdendritic regions, as identified by WDS (Fig. 5). This inconsistent non-equilibrium microstructure leads to a lack of reproducibility and predictability of properties when cold-sprayed, and this is particularly critical given cold spray repairs need a complete understanding and control of the deposit properties, and the absence of melting during the cold spay implies that the original state of the powder will be conserved in the deposits. Additionally, the solute-rich interdendritic regions have been shown to influence the coatings' response to post-deposition heat treatment (Ref 21). Thus, here, the powder was altered by solution heat treatment followed by quenching. SEM images of a particle of AA7075 after this process (Fig. 7) reveal that the solute atoms have been dissolved into a solid solution, and the matrix has been largely homogenized. Numerous phases were, however, observed in the microstructure. It has been suggested that, as the cooling rate undergone by the powder during quench after solution heat treatment, is probably too rapid for much diffusion to occur, the formation of the needle-shaped precipitates presumably occurred during the heat treatment itself. This is supported by the literature, which reveals that many phases can be expected to precipitate during a solution heat treatment, due to the low solubility of some of the components (in this case Cu and Fe) in Al (Ref 36). Phases like Al_7Cu_2Fe (Ref 27) and Al_2CuMg (Ref 37) have been observed at grain interiors and along the grain boundaries in wrought alloys, among others. The needle-shaped precipitates may be identified as Al_7Cu_2Fe which were formed during heat treatment from the Fe and Cu-rich areas of the as-received powder. Studies revealed that a well-solutionized wrought alloy contains only Al_7Cu_2Fe, $(Fe,Cr)_3SiAl_{12}$ as well as Mg_2Si (Ref 38). The high concentration of magnesium in some areas observed on the EPMA images combined with the dark contrasts observed in BSE could indicate the presence of Mg_2Si phases in the heat-treated powder. The Mg_2Si phase is potentially present in the original material, but is insoluble in the matrix, and tends to spheroidize during heat treatments (Ref 38).

However, fairly homogeneous microstructures are observed in the cases of the smaller particles (< 10 μm), either using optical microscopy (Fig. 6b) or backscattered SEM (Fig. 7b). This is associated with the finer dendritic structure exhibited by the small particles of as-received powder. Their weaker solute segregation gives less potential for the agglomerated Cu- and Fe-rich phases to form during heat treatment. Microhardness tests on both batches of powder revealed a link between the microstructural modification and the mechanical properties. The homogeneous microstructure obtained post-quench is associated with a 25% decrease in hardness, due to the redistribution of the alloying elements in the aluminum matrix. A dissolution of grain boundary precipitates is also considered, as a presence of those phases would potentially hinder the dislocation motion. The phases observed in the as-quenched microstructure (Fig. 7) of the studied material, coarse and numerous are believed to be non-coherent with the aluminum matrix, thus not altering its mechanical properties.

Particle Deformation and Cold-Sprayed Coatings

The cold spray experiments performed on both as-received and heat-treated powders revealed different behaviors. A high deformation was exhibited by the as-quenched powder, facilitating deposition, whereas the lack of deformation observed during swipe tests for the as-received powder led to a low coating deposition.

The particle bonding in cold spray is predominantly based on the ductility of the substrate and the sprayed material and specifically on their ability to deform plastically upon impact. The sprayed materials (Table 1) as well as the substrate (109 ± 5.4 HV) used in this study were relatively soft; thus, a soft/soft behavior was expected in both cases upon impact, according to the particle impact model proposed by Ref 39. However, the particles have to reach a so-called critical velocity in order to adhere to the substrate, which is based on several factors, and especially the size, temperature and thermomechanical properties of the sprayed material (Ref 2). Critical velocities for Al/Al were estimated to be 775 m s^{-1} for particles having an average size of 35 μm, being quite high due to the low density and high heat capacity of the material (Ref 39).

A large number of craters were observed for as-received powder swipe test, which exhibited an extremely low fraction of crater versus deposition (8.6%). Considered as

an illustration of a lack of bonding between the particles and the substrate (Ref 1), the craters observed on the surface of the substrate reveal that the incident particles tend to bounce back rather than stick to the substrate. This lack of bonding exhibited by the particles is also observed on the tilted SEM images (Fig. 10a). This is demonstrated by the gap observed below the powder particle as well as the weak deformation of the particle, which indicate that the velocities reached by the particle combined with its ability to deform are not enough to create a bonding with the substrate. However, we can observe significant deformation of the substrate (Fig. 10b). This suggests that an anchoring mechanism has occurred, where most of the plastic deformation is undergone by the substrate, leading to a deep penetration of the sprayed material retaining mostly a spherical shape. This phenomenon could potentially explain why only a few particles bonded. In the case of the softer solution heat-treated powder, different bonding is observed. In fact, almost half of the sprayed particles adhered to the substrate (49.6%), showing a better particle–substrate bonding.

The tilted SEM images of those particles (Fig. 10c, d) illustrate this different behavior, showing the heavy deformation undergone by the powder itself. Material jetting is observed on the side of the particle, showing the presence of an adiabatic shear instability phenomenon—typical of a high strain rate deformation upon impact, where thermal softening dominates over work hardening (Ref 40). The higher ductility of the powder post-heat treatment increases the ability of the powder to deform and thus lead to the formation of this ring of jet type morphology.

The bonding between the particles and the substrate was improved by the heat treatment performed on the 7075 series aluminum alloy powder, and the coating building up revealed that the bonding between the particles themselves was also enhanced. The 300-µm-thick (Fig. 11b) coating illustrates the improvement in bonding between the particles using the selected parameters. The same parameters used on the as-received powder led to only a few micrometers (Fig. 11a), showing that the rebounding effect observed during the swipe tests was also occurring when particles were impacting on other particles. In both cases, the interface between the substrate and the first layer of coating appears to be strong, and mechanical mixing at the interface is observed in the case of the sprayed as-received powder (Fig. 12b), indication of a good material interlocking (Ref 40). However, this apparent good bonding, in contrast with the swipe tests results, is believed to be due to the hammering of the incident incoming particles after the first layer. Indeed, once the first layer of particles stuck to the substrates, more particles are sprayed, and mostly not deposited, according to the observed coating thickness. Thus, a hammering effect occurs, which could be assimilated to an in-situ shot peening effect, which has been showed to decrease porosity and increase the cohesion of the coating (Ref 41). This suggestion is supported by the really fine dendritic structure observed at the particle–substrate interface. It contrasts with the much larger dendritic cells still observed at the top layer and illustrates the compression undergone by the particles in contact with the substrate, being the most compressed one. A good particle–particle cohesion as well as particle–substrate adhesion combined with the higher thickness is measured in the case of the sprayed solution heat-treated powder, showing the effect of the increase in ductility prior to deposition. Although the increase in the gas heating temperature has been showed to have an impact on cold spray deposition, lowering the critical velocity as well as helping the powder deformation upon impact (Ref 3), the spraying here has been performed at room temperature. It is argued that the solution heat treatment of the powder feedstock has essentially decreased the so-called critical velocity of the powder, which resulted in higher deposition efficiency, by altering the intrinsic micromechanical properties of the feedstock. A coating of a relative superior thickness was obtained in those conditions, showing the major importance of the ability of the sprayed material to deform.

In this work, the ductility of the sprayed powder was identified to be the main factor increasing the deposition efficiency and therefore coating build-up. It is not believed that the homogeneous microstructure and its Al-Zn matrix combined with the Cu-Fe phases obtained after heat treatment was the main contributor to this improvement of in-process deformation. However, the solution heat treatment of the material and its homogeneous microstructure offer good potential in terms of post-deposition coating aging. A low temperature aging (120 °C) could potentially develop a fine dispersion of strengthening precipitates in this solid solution matrix, thereby increasing mechanical properties.

Conclusions

In this study, the solution heat treatment (SHT) of gas-atomized 7075 series aluminum alloy powder was performed using a novel technique. As-received and SHT powders were cold-sprayed using swipe tests and coating deposition trials in order to understand the effect of the microstructural modification on the particle impact phenomena.

- The non-equilibrium microstructure of gas-atomized aluminum alloy powders, which is not ideal for cold spray deposition, was homogenized using a solution

heat treatment followed by quenching. The dendritic structure of the as-received powder was eliminated, and the solute atoms present in the powder were dissolved to form a uniform solid solution. Coarse Fe- and Cu-rich phases were formed during heat treatment due to the low solubility of the aforementioned elements in the aluminum matrix.

- Microhardness of the solution heat-treated powder feedstock was reduced by 25% due to the redistribution of the alloying elements in the matrix during the solution heat treatment.
- The lower microhardness of the solution heat-treated particles led to greater deformation of the particles during cold spray impacts on an AA6061 substrate, as evidenced by material jetting and by the shapes of the splats compared to the deformation of the as-received powder particles, implying a higher fraction of deposition.
- The high degree of deformation and the improved bonding between the particles were observed in coatings prepared from heat-treated powder feedstock. Under identical spraying parameters, a 300-µm-thick coating was obtained in the case of the heat-treated powder, showing a homogeneous microstructure, whereas only few layers of as-received powder were deposited, reaching only a 40-µm-thick coating exhibiting a dendritic microstructure.

Acknowledgments This work was supported by the Engineering and Physical Sciences Research Council [grant number EP/M50810X/1]; in the form of a CASE PhD studentship and industrial funding from TWI via the National Structural Integrity Research Foundation (NSIRC). The authors also acknowledge support from J. Murray for his editorial work, R. Screaton at the University of Nottingham for conducting the cold spray experiments and P. McNutt and M.D.F.H. Harvey at TWI for valuable technical discussions.

References

1. T. Schmidt, F. Gärtner, H. Assadi, and H. Kreye, Development of a Generalized Parameter Window for Cold Spray Deposition, *Acta Mater.*, 2006, **54**(3), p 729-742
2. H. Assadi, F. Gärtner, T. Stoltenhoff, and H. Kreye, Bonding Mechanism in Cold Gas Spraying, *Acta Mater.*, 2003, **51**(15), p 4379-4394
3. T. Schmidt, H. Assadi, and F. Gärtner, From Particle Acceleration to Impact and Bonding in Cold Spraying, *J. Therm. Spray Technol.*, 2009, **18**(5–6), p 794-808
4. V. Champagne and D. Helfritch, Critical Assessment 11: Structural Repairs by Cold Spray, *Mater. Sci. Technol.*, 2015, **31**(6), p 627-634
5. V.K. Champagne, D.J. Helfritch, M.D. Trexler, and B.M. Gabriel, The Effect of Cold Spray Impact Velocity on Deposit Hardness, *Model. Simul. Mater. Sci. Eng. Mater. Sci. Eng*, 2010, **18**(18), p 065011
6. Z. Arabgol, H. Assadi, T. Schmidt, F. Gärtner, and T. Klassen, Analysis of Thermal History and Residual Stress in Cold-Sprayed Coatings, *J. Therm. Spray Technol.*, 2014, **23**(1–2), p 84-90
7. V. Luzin, K. Spencer, and M.-X. Zhang, Residual Stress and Thermo-Mechanical Properties of Cold Spray Metal Coatings, *Acta Mater.*, 2011, **59**(3), p 1259-1270
8. F. Gartner, T. Stoltenhoff, J. Voyer, H. Kreye, S. Riekehr, and M. Kocak, Mechanical Properties of Cold-Sprayed and Thermally Sprayed Copper Coatings, *Surf. Coat. Technol.*, 2006, **200**(24), p 6770-6782
9. W.-Y. Li, C.-J. Li, and H. Liao, Effect of Annealing Treatment on the Microstructure and Properties of Cold-Sprayed Cu Coating, *J. Therm. Spray Technol.*, 2006, **15**(2), p 206
10. R. Huang, M. Sone, W. Ma, and H. Fukanuma, The Effects of Heat Treatment on the Mechanical Properties of Cold-Sprayed Coatings, *Surf. Coat. Technol.*, 2015, **261**, p 278-288
11. B. AL-Mangour, P. Vo, R. Mongrain, E. Irissou, and S. Yue, Effect of Heat Treatment on the Microstructure and Mechanical Properties of Stainless Steel 316L Coatings Produced by Cold Spray for Biomedical Applications, *J. Therm. Spray Technol.*, 2014, **23**(4), p 641-652
12. A. Zambon, B. Badan, A.F. Norman, A. Greer, and E. Ramous, Development of Solidification Microstructures in Atomized Fe-Ni Alloy Droplets, *Mater. Sci. Eng., A*, 1997, **226**, p 119-123
13. Y.E. Kalay, L.S. Chumbley, I.E. Anderson, and R.E. Napolitano, Characterization of Hypereutectic Al-Si Powders Solidified under Far-From Equilibrium Conditions, *Metall. Mater. Trans. A*, 2007, **38**(7), p 1452-1457
14. K. Drewes, K. Schaefers, M. Rösner-Kuhn, and M. Frohberg, Measurements of Dendritic Growth and Recalescence Rates in Undercooled Melts of Cobalt, *Mater. Sci. Eng., A*, 1998, **241**(1–2), p 99-103
15. M.R. Rokni, C.A. Widener, and V.R. Champagne, Microstructural Evolution of 6061 Aluminum Gas-Atomized Powder and High-Pressure Cold-Sprayed Deposition, *J. Therm. Spray Technol.*, 2014, **23**(3), p 514-524
16. M.R. Rokni, C.A. Widener, G.A. Crawford, and M.K. West, An Investigation into Microstructure and Mechanical Properties of Cold Sprayed 7075 Al Deposition, *Mater. Sci. Eng. A Struct. Mater. Prop. Microstruct. Process.*, 2015, **625**, p 19-27
17. S. He, Y. Liu, and S. Guo, Cooling Rate Calculation of Non-Equilibrium Aluminum Alloy Powders Prepared by Gas Atomization, *Rare Met. Mater. Engineering*, 2009, **38**, p 353-356
18. C.J. Kong, P.D. Brown, S.J. Harris, and D.G. McCartney, Analysis of Microstructure Formation in Gas-Atomised Al–12wt.% Sn–1wt.% Cu Alloy Powder, *Mater. Sci. Eng., A*, 2007, **454**, p 252-259
19. J.D. Hunt et al., Numerical Modeling of Cellular/Dendritic Array Growth: Spacing and Structure Predictions, *Metall. Mater. Trans. A*, 1996, **27**(3), p 611-623
20. G.K. Sigworth, Fundamentals of Solidification in Aluminum Castings, *Int. J. Met.*, 2014, **8**(1), p 7-20
21. M.R. Rokni, C.A. Widener, V.K. Champagne, and G.A. Crawford, Microstructure and Mechanical Properties of Cold Sprayed 7075 Deposition During Non-isothermal Annealing, *Surf. Coat. Technol.*, 2015, **276**, p 305-315
22. J.E. Hatch, *Aluminum Properties and Physical Metallurgy*, ASM International, William Park Woodside, 1984

23. Structural Aluminum Cold Spray Development. [Online]. http://www.coldsprayteam.com/T12 Nardi CSAT-2016 062116.pdf. Accessed 25 Sep 2017.
24. Z.-Y. Cai, C. Zhang, R.-C. Wang, C.-Q. Peng, K. Qiu, and N.-G. Wang, Effect of Pre-annealing on Microstructure and Compactibility of Gas-Atomized Al – Si Alloy Powders, *Trans. Nonferrous Metals Soc. China*, 2016, **26**, p 2355-2362
25. T. Hussain, D.G. Mccartney, and P.H. Shipway, Impact Phenomena in Cold-Spraying of Titanium onto Various Ferrous Alloys, *Surf. Coat. Technol.*, 2011, **205**, p 5021-5027
26. S. Özbilen, Satellite Formation Mechanism in Gas Atomised Powders, *Powder Metall.*, 1999, **42**(1), p 70-78
27. W. Feng, X. Baiqing, Z. Yongan, H. Liu, and H. Xiaoqing, Microstructural Development of Spray-Deposited Al–Zn–Mg–Cu Alloy During Subsequent Processing, *J. Alloys Compd.*, 2009, **477**, p 616-621
28. H. Jones, Microstructure of Rapidly Solidified Materials, *Mater. Sci. Eng.*, 1984, **65**(1), p 145-156
29. G. Von Bradsky and R.A. Ricks, Solidification Microstructures in Rapidly Solidified, Gas Atomized Aluminium-Lithium Alloy Powders, *J. Mater. Sci.*, 1987, **22**, p 1469
30. Y. Birol, F. Birol, B. Yuksel, and O. Duygulu, Corrosion Behaviour of Twin Belt Cast EN AW 7075 alloy, *Mater. Corros.*, 2012, **64**(10), p 881-889
31. D.S. MacKenzie and G.E. Totten, *Analytical Characterization of Aluminum, Steel, and Superalloys*, CRC Press, London, 2005, p 111-125
32. T. Hussain, D.G. Mccartney, P.H. Shipway, and D. Zhang, Bonding Mechanisms in Cold Spraying: The Contributions of Metallurgical and Mechanical Components, *J. Therm. Spray Technol.*, 2009, **18**(3), p 364-379
33. S. Hariprasad, S.M.L. Sastry, and K.L. Jerina, Undercooling and Supersaturation of Alloying Elements in Rapidly Solidified Al-8.5% Fe-1.2% V-1.7% Si Alloy, *J. Mater. Sci.*, 1996, **31**(4), p 921-925
34. O.D. Neikov, I.B. Murashova, N.A. Yefimov, and S. Nabocychenko, *Handbook of Non-Ferrous Metal Powders : Technologies and Applications*, Elsevier, London, 2008, p 554-558
35. R. Haghayeghi, *Grain Refinement and Nucleation Processes in Aluminum Alloys Through Liquid Shearing*, Brunel University, London, 2009
36. G.E. Totten and D.S. MacKenzie, *Handbook of Aluminium, Volume 1: Physical Metallurgy and Processes*, Vol 7, CRC Press, New York, 2003, p 121-123
37. M.R. Rokni, A. Zarei-Hanzaki, and H.R. Abedi, Microstructure Evolution and Mechanical Properties of Back Extruded 7075 Aluminum Alloy at Elevated Temperatures, *Mater. Sci. Eng., A*, 2011, **532**, p 593-600
38. J.R. Davis, ASM International, Handbook Committee et al., *Aluminum and Aluminum Alloys*, ASM International, William Park Woodside, 1993, p 494-508
39. G. Bae, Y. Xiong, S. Kumar, K. Kang, and C. Lee, General Aspects of Interface Bonding in Kinetic Sprayed Coatings, *Acta Mater.*, 2008, **56**, p 4858-4868
40. T. Hussain, D.G. McCartney, and P.H. Shipway, Bonding Between Aluminium and Copper in Cold Spraying: Story of Asymmetry, *Mater. Sci. Technol.*, 2012, **28**(12), p 1371-1378
41. X.-T. Luo, Y.-K. Wei, Y. Wang, and C.-J. Li, Microstructure and Mechanical Property of Ti and Ti6Al4 V Prepared by an In-Situ Shot Peening Assisted Cold Spraying, *Mater. Des.*, 2015, **85**, p 527-533